INSTITUTE OF PHYSICS PUBLISHING JOURNAL OF PHYSICS: CONDENSED MATTER

J. Phys.: Condens. Matter **15** (2003) 6031–6041 PII: S0953-8984(03)63939-1

Composition variation and the monoclinic phase within $Pb(Zr_xTi_{1-x})O_3$ ceramics

J Frantti[1,5], S Eriksson[3], S Hull[2], V Lantto[4], H Rundlöf[3] and M Kakihana[1]

[1] Materials and Structures Laboratory, Tokyo Institute of Technology, 4259 Nagatsuta, Midori-ku, Yokohama 226-8503, Japan
[2] The ISIS Facility, Rutherford Appleton Laboratory, Chilton, Didcot, Oxfordshire OX11 0QX, UK
[3] Studsvik Neutron Research Laboratory, Uppsala University, SE-611 82, Nyköping, Sweden
[4] Microelectronics and Materials Physics Laboratories, University of Oulu, Linnanmaa, PO Box 4500, FIN-90014 University of Oulu, Finland

E-mail: jfrantt1@msl.titech.ac.jp

Received 27 May 2003, in final form 15 July 2003
Published 22 August 2003
Online at stacks.iop.org/JPhysCM/15/6031

Abstract
High-resolution neutron powder diffraction data were collected from a $Pb(Zr_{0.54}Ti_{0.46})O_3$ powder sample. Data were analysed using Rietveld refinement. The diffraction patterns showed the presence of two 'coexisting' phases, which had the rhombohedral $R3c$ and monoclinic Cm symmetries at 4 K. A phase transformation between the $R3c$ and Cm phases occurred as a function of temperature. The Bragg peaks of the Cm phase showed strongly reflection-indices-dependent line broadening due to the spatial variation of the Zr/Ti ratio, δx. This was modelled using a microstrain broadening form developed by Stephens (1999 *J. Appl. Crystallogr.* **32** 281). Constant microstrain surfaces were plotted for each phase at different temperatures and the microscopic changes responsible for the observed changes were identified. The phase of Cm symmetry is reproducibly absent in the limit of $\delta x = 0$.

(Some figures in this article are in colour only in the electronic version)

1. Introduction

A class of materials possessing high piezoelectric coefficients and electromechanical coupling factors are the $AB_xB'_{1-x}O_3$ type perovskites, where the B-cation site is occupied by two or three kinds of cations. The composition ratio between the B cations is often adjusted so that it corresponds to a phase boundary, typically separating rhombohedral and tetragonal

[5] Author to whom any correspondence should be addressed.

phases. Examples are xPb($Mg_{1/3}Nb_{2/3}$)O_3–$(1-x)$ $PbTiO_3$ (PMN–PT), xPb($Zn_{1/3}Nb_{2/3}$)O_3–$(1-x)$ $PbTiO_3$ (PZN–PT) and Pb(Zr_xTi_{1-x})O_3 (PZT) solid solutions. The first two can be prepared in a single-crystal-like form (strictly speaking, they are not single crystals as they contain crystal volumes with different symmetries, such as tetragonal and rhombohedral), while the bulk PZT is virtually always prepared in the form of polycrystalline ceramics. A fundamental understanding of the excellent piezoelectrical properties of these materials is still needed, although 'polarization rotation' theory, developed for $BaTiO_3$, is commonly invoked to explain the piezoelectric properties of these solid solutions [1]. This theory misses the important consequences of the compositional and structural disorder present in solid solutions. High-resolution x-ray synchrotron diffraction experiments revealed that PZT samples with x in the vicinity of the morphotropic phase boundary (MPB) contain a monoclinic phase (space group Cm) [2–4], and similarly a monoclinic Pm phase was reported to exist between the rhombohedral and tetragonal symmetries in PMN–PT [5] and PZN–PT [6]. The phase fraction of the Cm phase in PZT depends on both the average composition x and temperature [7]. In addition, neutron powder diffraction (NPD) patterns revealed that there were two 'coexisting' phases, with space groups $R3c$ and Cm. This coexistence is due to the spatial variation of x (labelled as δx) and should be distinguished from the thermodynamical coexistence of phases characteristic of first-order phase transitions. It was also reported that the Cm phase in PZT ceramics relieves the stress which would be generated due to the interacting $R3m$ and $P4mm$ phases in the vicinity of the MPB [8].

Our aim was to study the temperature and composition dependence of the structural details of PZT ceramics in the vicinity of the MPB by experimental means and to find a microscopic description for the observed phase transition sequence. This report is also intended to be a case study illustrating how one can also extract useful information from the diffraction peak profiles in the case of other crystalline materials. For this purpose, the following three conditions were crucial: (i) high resolution, (ii) sensitivity to the oxygen positions and (iii) whole pattern fitting.

2. Experimental details

2.1. Sample preparation and data collection

PZT with $x = 0.54$ was prepared through the conventional solid state reaction (SSR) technique [7]. Although sol–gel type techniques are often preferred to yield highly homogeneous samples, in the case of PZT powders they have certain drawbacks compared to the SSR technique. Most serious is the significant composition fluctuation resulting in two-phase coexistence already in the case of $x \leqslant 0.50$ [9]. To our knowledge, no single-phase PZT samples with compositions in the vicinity of the MPB have been prepared. Somewhat surprisingly, samples prepared through the SSR technique seem to be closest to this limit. In addition, the data obtained from samples prepared through the SSR technique by different groups seem to be consistent with each other.

The high resolution powder diffractometer (HRPD) at the Rutherford Appleton Laboratory was used for the collection of the NPD data. As the resolution of HRPD is high ($\Delta d_{hkl}/d_{hkl} = 10^{-4}$, where d_{hkl} is the distance between the (hkl) lattice planes), it is well suited to the study of the hkl-dependent line broadening. Further, the resolution $\Delta d_{hkl}/d_{hkl}$ is approximately constant with d_{hkl}, thus allowing precise structural refinements. Data collected at the backscattering bank were used. A closed cycle helium cryostat and a furnace were used for the low- and high-temperature measurements, respectively. The general structure analysis system (GSAS) was used for the Rietveld refinements [10].

2.2. Modelling the anisotropic strain broadening

To model the peak profiles, we used the GSAS lineshape 4 [10, 11] which takes the microstrain contribution phenomenologically into account. Microstrain broadening is described by the parameters S_{HKL} and the widths of the Bragg reflection peaks are proportional to the factor $S_S(hkl) = d_{hkl}^2\sqrt{\sum_{HKL} S_{HKL}h^H k^K l^L}/C$, where the indices H, K and L are constrained to fullfil the condition $H + K + L = 4$ and where C is the diffractometer constant ($C = 48\,235.58\ \mu\text{s Å}^{-1}$). The number of S_{HKL} parameters is limited by the crystal symmetry [11], so that for the cubic, monoclinic and rhombohedral symmetries one can write [10]

$$S_S(hkl) = \begin{cases} \dfrac{d_{hkl}^2}{C}[S_{400}(h^4 + k^4 + l^4) + 3S_{220}(h^2k^2 + h^2l^2 + k^2l^2)]^{1/2} \\ \quad \text{(Laue symmetry } m\bar{3}m) \\ \dfrac{d_{hkl}^2}{C}[S_{400}h^4 + S_{040}k^4 + S_{004}l^4 + 3(S_{220}h^2l^2 + S_{202}h^2k^2 + S_{022}k^2l^2) \\ \quad + 2(S_{301}h^3l + S_{103}hl^3) + 4S_{121}hk^2l]^{1/2} \qquad \text{(Laue symmetry } 2/m) \\ \dfrac{d_{hkl}^2}{C}[S_{400}(h^4 + k^4 + 3h^2k^2 + 2h^3k + 2hk^3) + S_{004}l^4 \\ \quad + 3S_{202}(h^2l^2 + k^2l^2 + hkl^2) + S_{301}(3h^2kl - 3hk^2l + 2h^3l - 2k^3l)]^{1/2} \\ \quad \text{(Laue symmetry } \bar{3}m1\text{, hexagonal setting)} \end{cases}$$

3. Results and discussion

As the diffraction peaks of the $R3c$ and Cm phases were overlapping (with a few exceptions) Rietveld refinement (a fitting of the whole diffraction pattern by the same set of parameters, instead of fitting a few individual peaks) was an invaluable method for the determination of the hkl-dependent line broadening. As a result of the refinement we obtained the S_{HKL} parameters for each symmetry under consideration. Tables 1 and 2 give the lineshape and structural data, respectively, extracted from the $x = 0.54$ sample at different temperatures. Weight fractions were determined by the GSAS software, which also provided the standard errors (for details, see [10], p 136). The goodness-of-fit numbers χ^2, R_{wp}, R_p, R_{wpb} and R_{pb} are defined in the GSAS manual [10] on p 168. We realized that R values have been a subject of numerous discussions [12–14] and that a definition of 'universally' valid R values is difficult. In our experience, even the same structural model for the data collected on the same samples at the same ambient conditions using different instruments (say, constant wavelength neutron powder diffractometer versus the present HRPD instrument) may yield somewhat different R values, although the structural data extracted were almost the same. After recognizing this difficulty, we decided to report the details (such as bond lengths) of the structure and to show that they are reasonable. In addition, the statistics were good, which was ensured by long data collection times.

We plotted constant $\sum_{HKL} S_{HKL}h^H k^K l^L \equiv S_S$ surfaces for the $Pm\bar{3}m$, $R3c$ and Cm phases in figure 1, i.e. solely the microstrain contribution is shown. The key result is that there were three nonequivalent cone pairs (cones of a pair are equivalent as each reciprocal lattice has an inversion symmetry) in the case of the Cm phase at 4, 135 and 295 K. Drastic changes occur once the sample is heated to 583 K: the S_S surface of the Cm phase is now a 'distorted ellipsoid'. For an easier visualization, we also plotted closed surfaces for the Cm phase at 4, 135 and 295 K. This was done by replacing the reciprocal $\boldsymbol{b}^*$ axis by a corresponding imaginary axis $\mathrm{i}\boldsymbol{b}^*$ (which was easiest to do by reversing the sign of the S_{202}, S_{022} and S_{121} parameters, see also table 1 and the equation given above for the $S_S(hkl)$ values of the monoclinic phase). The open and closed surfaces contain identical information, although the interpretation of the

Table 1. Microstrain parameters S_{HKL} in the case of the 0.54 sample at different temperatures. If a standard error value is not indicated, it means that this parameter was fixed during the refinement. η is a 'mixing coefficient' which determines the contributions of the Gaussian and Lorentzian broadening [10]. Cases $\eta = 0$ and 1 correspond to the pure Gaussian and Lorentzian lineshapes, respectively. The other profile parameters were the instrument parameters $\alpha = 0.1359$, $\beta_0 = 0.021\,086$ and $\beta_1 = 0.011\,943$, which were kept locked during the refinement and were determined by the instrument scientists at ISIS.

T (K)	4	135	295	583	773
	Cm	Cm	Cm	Cm	$Pm\bar{3}m$
η	0.4541(17)	0.330(23)	0.3512(69)	0.7141(75)	0.7810(45)
S_{400}	105(5)	76(5)	26.56(58)	8.23(34)	12.56(12)
S_{040}	47(2)	48(3)	26.87(57)	2.91(15)	
S_{004}	686(30)	575(29)	343(5)	28.10(58)	
S_{220}	97(3)	80(3)	36.38(52)	3.59(12)	6.22(10)
S_{202}	−175(8)	−131(8)	−45(1)	−1.55(51)	
S_{022}	−112(5)	−106(6)	−52(1)	−0.76(25)	
S_{301}	−27(3)	−34(3)	−38.05(65)	−8.03(51)	
S_{103}	59(9)	94(11)	120(2)	13(1)	
S_{121}	10(3)	−2(3)	−12.63(71)	−0.49(38)	
	$R3c$	$R3c$	$R3c$	$R3c$	
η	0.14(3)	0.149(31)	0	0	
S_{400}	5.4(3)	5.04(27)	3.87(17)	4.23(24)	
S_{004}	0.0270(18)	0.0257(18)	0.0156(14)	0.360(41)	
S_{202}	5.21(27)	5.17(27)	8.04(24)	4.73(17)	
S_{301}	0	0	0	0	

open surface is easier. At the same time, the constant S_S surfaces of the $R3c$ phase were 'distorted ellipsoids', which were largely independent of temperature (although an elongation along the reciprocal lattice $\boldsymbol{c}^*$ axis is seen). Thus, when the constant strain surfaces are plotted against $\boldsymbol{a}^*$, $\boldsymbol{b}^*$ and $\boldsymbol{c}^*$ axes, it is seen that, for reflection indices located inside a cone or outside an 'ellipsoid' surface (further from the origin), the microstrain broadening exceeds the given constant value (here 0.05 or 0.005, depending on the phase and temperature, see figure 1). Thus, the 'cone axes' are the softest crystal directions: corresponding d_{hkl} values are the most susceptible to spatial inhomogeneities. By selecting a sufficiently small value for this constant (too large a value corresponds to too large values of hkl that the microstrain broadening cannot be experimentally verified) one can conveniently classify the reflections according to their microstrain broadening even in the case of hundreds of reflections. The benefit of the present method is that not only the changes of the lattice parameters are studied, but virtually all reciprocal lattice vectors are checked. Correspondingly, plots such as those shown in figure 1 visualize the variation of lattice plane distances, δd_{hkl}, against δx. We note that the representation quadric cannot accommodate this type of behaviour, which explains why the GSAS lineshape 4 was found to be superior to lineshape 3. The latter describes the microstrain by 6 L_{ij} parameters and the representation quadric as either an ellipsoid or a hyperboloid of one or two sheets.

3.1. Origin of the anisotropic strain broadening

To understand the reasons underlying the phase transition sequence $P4mm \rightarrow Cm \rightarrow R3c$ and the strongly hkl-dependent line broadening of the Cm phase, in contrast to the order-of-magnitude narrower linewidths of the $R3c$ phase, we computed the O–O bond lengths of $0.20 \leqslant x \leqslant 0.54$ samples. Selected bond lengths versus x at low temperature are shown in figure 2(a). The O–O bond lengths of the $x = 0.54$ sample versus temperature are shown in

Table 2. Structural data and statistical figures of merit for the $x = 0.54$ sample. Lattice parameters and fractional coordinates of the $R3c$ phase refer to the hexagonal setting. During the refinements, either Pb ions (space groups Cm and $Pm\bar{3}m$) or Zr/Ti ions (space group $R3c$) were fixed at the origin. In addition, the four thermal displacement parameters of Zr and Ti in the Cm and $R3c$ phases were constrained to be the same, since the oxygen octahedra of both phases were similar (particularly at low temperatures). At 583 K, the symmetry $R3c$ was used together with the constraint $y(O) = 2x(O)$, which corresponds to the $R3m$ symmetry (see [7, 15]).

T (K)	4	4	135	135	295	295	583	583	773
	Cm	$R3c$	Cm	$R3c$	Cm	$R3c$	Cm	$R3c$	$Pm\bar{3}m$
a (Å)	5.751 76(42)	5.738 000(68)	5.753 52(43)	5.742 104(64)	5.748 46(14)	5.755 80(12)	5.743 819(65)	5.763 59(18)	4.080 168(6)
b (Å)	5.722 45(32)		5.725 91(35)		5.730 94(13)		5.745 756(58)		
c (Å)	4.096 00(43)	14.199 65(24)	4.098 18(45)	14.202 14(23)	4.109 36(14)	14.196 58(34)	4.107 554(28)	14.172 1(15)	
β (deg)	90.534(2)		90.505(3)		90.426(1)		90.076(1)		
U_{iso}(Pb) (Å^2)	0.0054(11)	0.0075(11)	0.0109(16)	0.0093(12)	0.0262(6)	0.0137(15)	0.0410(8)	0.0254(34)	0.0524(4)
U_{iso}(Ti, Zr) (Å^2)	0.0059(9)	0.0059(9)	0.0068(9)	0.0068(9)	0.0063(6)	0.0063(6)	0.0116(6)	0.0116(6)	0.0126(6)
$U_{iso}(O_1)$ (Å^2)	0.0096(20)		0.0101(23)		0.0167(8)		0.0267(8)		
$U_{iso}(O_{2,3})$ (Å^2)	0.0120(14)	0.0042(7)	0.0116(17)	0.0061(8)	0.0175(6)	0.0125(12)	0.0237(5)	0.0194(20)	0.0335(2)
z (Pb)		0.2705(10)		0.2749(10)		0.2774(15)		0.2662(19)	
x (Zr/Ti)	0.4804(43)		0.4782(53)		0.4740(17)		0.4915(30)		
z (Zr/Ti)	0.5726(37)		0.5465(46)		0.5457(14)		0.5381(13)		
$x(O_1)$	0.4596(15)		0.4638(18)		0.4652(7)		0.4860(14)		
$z(O_1)$	0.0792(19)		0.0780(21)		0.0796(7)		0.0646(7)		
$x(O_{2,3})$	0.2101(11)	0.1497(5)	0.2132(13)	0.1555(5)	0.2159(5)	0.1627(9)	0.2404(11)	0.1742(7)	
$y(O_{2,3})$	0.2442(12)	0.3441(7)	0.2458(14)	0.3445(7)	0.2453(5)	0.3452(10)	0.2490(10)	0.3485(13)	
$z(O_{2,3})$	0.6083(14)	0.0680(10)	0.6032(16)	0.0729(11)	0.5991(6)	0.0759(15)	0.5765(6)	0.0729(25)	
Weight fraction (%)	0.5756(14)	0.4244(56)	0.5587(14)	0.4413(55)	0.8345(3)	0.1655(38)	0.8548(2)	0.1452(31)	1
χ^2	2.481		2.352		2.216		1.842		2.217
R_{wp} (%)	4.65		4.69		7.17		4.29		4.55
R_{wpb} (%)	4.97		5.18		5.81		4.26		5.22
R_p (%)	4.54		5.17		5.70		3.94		4.03
R_{pb} (%)	5.01		6.40		4.79		3.92		4.65

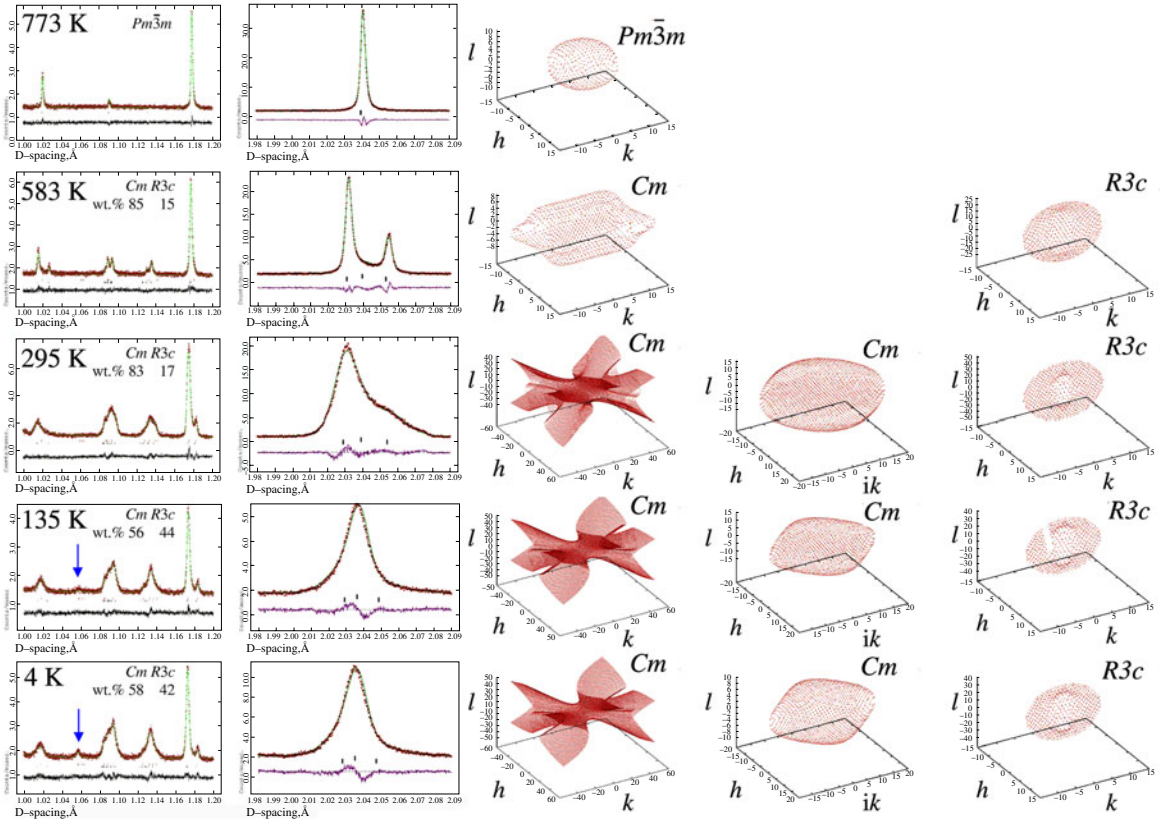

Figure 1. Left-hand column shows the low d-spacing regime. In the 4 and 135 K data reflections corresponding to an oxygen octahedra tilt allowed in the $R3c$ phase are indicated by an arrow, see [7] and figure 3. Second column from left: monoclinic (220) and (002) (lower tick marks) and rhombohedral ($20\bar{4}$) (upper tick mark) and cubic (200) (773 K data) reflections. Constant $\sum_{HKL} S_{HKL} h^H k^K l^L$ surfaces of the $x = 0.54$ sample at various temperatures in the case of the $Pm\bar{3}m$ (773 K), and 'coexisting' Cm and $R3c$ phases (583, 295, 135 and 4 K) are shown. For all plots, $\sum_{HKL} S_{HKL} h^H k^K l^L = 0.005$, except the Cm phase at 4, 135 and 295 K, for which the constant was 0.05. The phase fractions, in weight per cent, of the Cm and $R3c$ phases are indicated in the left-hand column.

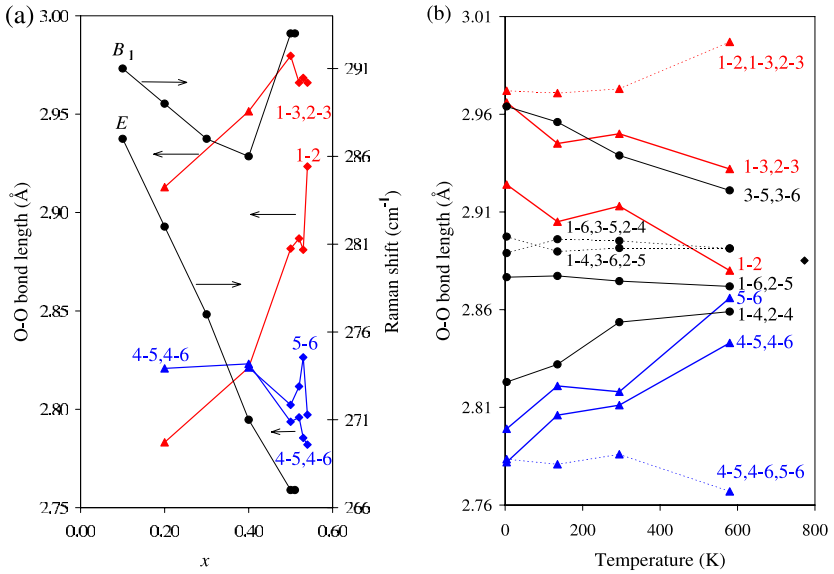

Figure 2. (a) Selected oxygen octahedra lengths of the $P4mm$ (triangles) and Cm (diamonds) phases. Data for the $x = 0.50$ sample (10 K) are from [17], for the $x = 0.52$ and 0.53 samples (10 K) from [7], and the Raman data (circles) are from [16]. Data from the $x = 0.20$ and 0.54 samples were collected at ISIS (4.2 K) and from the $x = 0.40$ sample (10 K) at Studsvik. (b) Oxygen octahedra edge lengths of the $R3c$ and Cm phases of the $x = 0.54$ sample versus temperature using the labelling given in figure 3. Full and broken lines correspond to the Cm and $R3c$ phases, respectively, and the 773 K datum corresponds to the $Pm\bar{3}m$ phase.

figure 2(b). Figure 3 specifies the bond lengths of interest and also shows the relationship between the $P4mm$, Cm and $R3c$ phases.

In the $P4mm$ phase, the a axis increases significantly with increasing x (indicated by the arrows A in figure 3) for $x \leqslant 0.50$ [7]. In the vicinity of the MPB the c axis also starts to decrease strongly (arrows B in figure 3). This is due to the B cations (most notably Zr), which shift towards the larger oxygen triangle 123 and which thus break the tetragonal symmetry (arrow C in figure 3). This shift allows oxygens 3 and 4 to approach each other. In addition, the distance between the triangles 123 and 456 increases with increasing x. Finally, at $x \approx 0.50$ the symmetry changes: the distance between the B cation and triangle 456 is so large that the bond length 4–6 starts to decrease with increasing x, while the lengths of bonds 1–2, 1–3 and 2–3 increase continuously with increasing x, as figure 2(a) demonstrates. In the Cm phase the bond length 1–2 increases fastest so that at $x = 0.54$ its length is almost equal to the bond lengths 1–3 and 2–3. Important changes are seen in bonds 1–2 and 5–6: they are equivalent by symmetry in the $P4mm$ phase, but differ in the Cm and $R3c$ phases. The difference between their bond lengths for the $x = 0.50$ sample at 10 K was 0.08 Å. This agrees with the low-temperature Raman observations of the B_1 mode (which involves only oxygens 1, 2, 5 and 6 in the case of the $P4mm$ symmetry: oxygens 1 and 5 vibrate in phase while oxygens 2 and 6 vibrate out of phase). The frequency of the B_1 mode first decreases with increasing x, and abruptly increases when x changes from 0.40 to 0.50 [17, 18], see figure 2(a). In contrast, the E-symmetry mode involves the vibrations of cations and anions in the tetragonal ab plane and its frequency decreases with increasing average B-cation mass and a-axis length. The same phenomenon was observed in $Pb(Hf_xTi_{1-x})O_3$ samples [19].

Basically, this type of distortion leads to the rhombohedral symmetry, which is achieved by forming two equilateral and coplanar oxygen triangles (in the case of the $P4mm$ phase, the

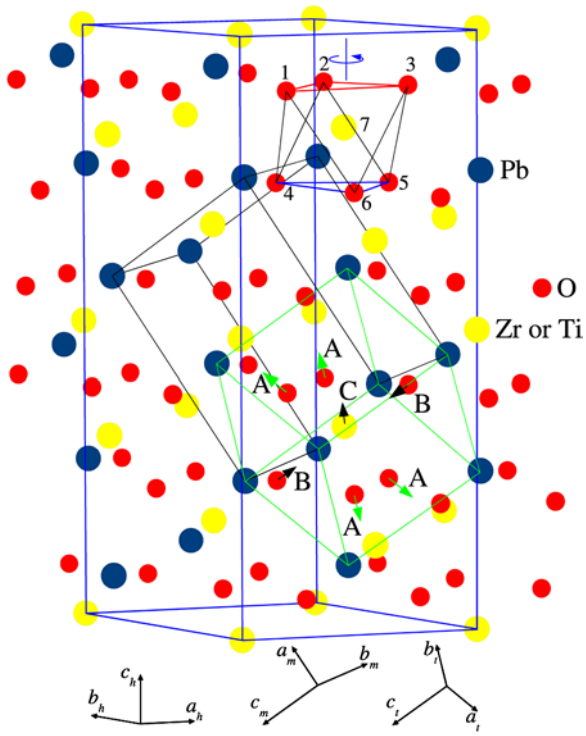

Figure 3. Relationship between the $P4mm$, Cm and $R3c$ phases. Black lines show the Cm unit cell, blue lines show the $R3c$ unit cell (hexagonal setting) and green lines show the $P4mm$ unit cell. The two almost equilateral oxygen triangles are indicated by blue lines (short edge) and by red lines (long edge). A schematic description of the changes occurring with increasing x in each phase are indicated by arrows: green arrows describe the shifts in the $P4mm$ phase, black lines in the Cm phase and the blue curved arrow describes the octahedral tilt occurring in the $R3c$ phase.

angle between the normals of the triangles 123 and 456 was $\approx 1.5°$ for $x < 0.50$): the larger one is formed once the B cation approaches the 123 triangle (so that they form a tetrahedron) and the smaller one is formed once the distance between the B cations and triangle 456 increases. Figure 2(b) shows that the octahedra edge lengths formed between triangles 123 and 456 (bonds 1–4, etc) of the $R3c$ phase were almost constant versus temperature and that the edge lengths of triangles 123 and 456 of the Cm phase were approaching the corresponding edge lengths of the $R3c$ phase. There is a tendency of the O–O bond lengths to become more equal with decreasing temperature, as figure 2(b) demonstrates. Further, it is the rhombohedral and not the monoclinic distortion which is experimentally found to be preferred once the interaction between oxygen and the B cations increases (as is the case once the crystal contracts with decreasing temperature). This is clearly seen in the strongly temperature-dependent phase fraction between the $R3c$ and Cm phases, as figure 1 shows. This result is in contrast with [3] where no phase transition between the Cm and rhombohedral phase was observed. This might be due to the fact that individual peaks were studied in [3]. On the other hand, some distinguishing reflections have almost zero intensity in the case of x-rays (especially those related to oxygen octahedra tilts), while they are clearly seen in NPD patterns.

This also explains the hkl-dependent line broadening of the Cm phase: there is a distribution of bond lengths (among bonds which ideally should be equivalent by symmetry)

due to the inhomogeneities, such as $\delta x \neq 0$, which hinder the development of the $R3c$ phase. With decreasing temperature the average bond lengths become shorter and finally the crystal is forced to adopt the $R3c$ symmetry. It is worth noting that the superlattice reflections are seen only at the lowest measurement temperatures, which indicates that the disorder increases rapidly with increasing temperature.

3.2. Comparison of homogeneity between our samples and previously studied samples

As the role of spatial inhomogeneities is significant for the understanding of PZT ceramics (and also for the related solid solutions), it is relevant to compare our samples with the other samples prepared through a similar sample preparation route (a comparison between the present and samples prepared through the sol–gel technique is somewhat obscured by the fact that the latter technique seems to have difficulties in reproducing similar PZT samples from time to time).

A rough estimate of sample homogeneity can be obtained by comparing reflection widths. In what follows we estimate the total peak widths. To allow a comparison between our samples and samples studied in [4] the same Bragg reflections of the samples with the same x (note that our x is equal to $1 - x$ used in [4]) at the same temperature should be compared. Although a strict comparison is not possible, as different reflections are shown at different temperatures in [4] for different samples, it can be seen that the line broadening shown in their figures 2 and 5 is very similar to ours. For example, the full width at half-maximum (FWHM) value of the reflection at 461 K (see [4], figure 5) is almost 0.015 Å, which is very close to the widest peak value in our figure 1. It is noteworthy that at 583 K the FWHM value of these reflections was only 20% from their low-temperature values (see figure 1). In addition, [4] mentions a low-temperature superlattice reflection observed in the case of a $Pb(Zr_{0.52}Ti_{0.48})O_3$ sample, which is consistent with our observation [7]. Although the exact amount of inhomogeneities depends on the sample preparation route we feel confident that the results and method described here have broad applicability.

3.3. Connection between the anisotropic strain and elastic properties

A very recent uniaxial compression study of a $Pb(Zr_{0.51}Ti_{0.49})O_3$ sample, carried out using neutron powder diffraction, indicated that the rhombohedral phase is more easily reoriented under the mechanical stress and electric field than the tetragonal phase [20]. As our sample had different average compositions (so that the phase fraction of the rhombohedral phase was larger, and instead of the tetragonal phase we had the Cm phase), strict comparison is difficult. In addition, an x-ray powder diffraction study of a $Pb_{0.94}Sr_{0.06}(Zr_{0.53}Ti_{0.47})O_3$ sample indicated that the tetragonal domains are rotated more easily than the rhombohedral domains under the electric field [21], which was described to be due to the larger spontaneous polarization of the rhombohedral phase. The depoling results for the rhombohedral phases reported in [20] and [21] were similar, but differed, possibly due to the different sample compositions, for the case of the tetragonal phase.

However, a comparison between the Cm and $R3c$ phases can be done, although the spatial composition variation δx cannot be treated similar to the true thermodynamical variables, such as pressure and temperature. On the other hand, it is clear that the phase fractions between the two coexisting phases are affected by the external pressure and electric field. Whether the phase transformations are reversible or not is apparently of further interest, but cannot be judged from the present data. Basically, one may anticipate that the directions which are most susceptible against δx might also be the softest crystal directions against external pressure. Nevertheless, it is useful to collect some remarks from the constant strain surfaces shown in figure 1. This can be done in an analogous way to the case of the representation quadric. In the

case of the real valued ellipsoid the microstrain broadening is largest in the directions where the surface is closest to the origin. For example, the shortest semiaxis of the ellipsoid of the $R3c$ phase at 4 K was approximately parallel to the $2(\boldsymbol{a}^* + \boldsymbol{b}^*) + \boldsymbol{c}^*$ direction (using hexagonal setting), while the longest axis was almost parallel to the $\boldsymbol{c}^*$ axis. This further indicates that the hexagonal c axis (pseudocubic $\langle 111 \rangle$ direction) is hardest against δx.

Due to the rather complicated shape of the constant strain surfaces of the Cm phase at 4, 135 and 295 K a detailed analysis was not straightforward to do. In the case of the Cm symmetry at 4, 135 and 295 K the most pronounced feature was that the overall broadening is an order of magnitude larger than in the case of the $R3c$ phase. In addition, it is the change of the parameters S_{202}, S_{022} and S_{121} which are responsible for the large changes observed at low temperatures, as was demonstrated in figure 1. At 583 K, the strain broadening was significantly lower than at lower temperatures. The largest anisotropic microstrain broadening was along the $\boldsymbol{c}^*$ axis direction, while the smallest broadening was along the $11\boldsymbol{a}^* + 13\boldsymbol{b}^* + 5\boldsymbol{c}^*$ direction.

Somewhat interestingly, the largest anisotropic strain broadening of the $Pm\bar{3}m$ phase was along the cube axes, while the smallest broadening was along the cubic face diagonals. This is consistent with the observation that the cubic phase first transforms to a tetragonal (the monoclinic distortion observed at 583 K was so small that the symmetry was almost tetragonal, see table 2) phase. Thus, information concerning the forthcoming symmetry is already present at the cubic phase.

4. Conclusions

A Rietveld study of high resolution neutron powder diffraction lineshapes was carried out. Reflection-indices-dependent line broadening was assigned to the spatial composition variation δx. A method where constant anisotropic strain values were plotted in a reciprocal lattice was used and is believed to suit the study of other solid solutions. Our interpretation is that the Cm phase is a result of frozen-in defects, most notably due to the inhomogeneous distribution of Zr and Ti ions. This is to be expected in the vicinity of the phase boundary between two symmetries, rhombohedral and tetragonal $P4mm$, which do not share a group–subgroup relationship, but which are energetically almost as favourable. Significantly temperature-dependent phase fractions indicated that a phase transformation between the $R3c$ and Cm phases occurred. The Cm phase is predictably absent in the case of $\delta x = 0$.

Acknowledgments

Dr Robert Von Dreele is acknowledged for his useful suggestions concerning the Rietveld refinement. One of us (JF) is grateful to the Academy of Finland (project no 44588) and Japan Society for the Promotion of Sciences for financial support (contract no 13001738).

References

[1] Fu H and Cohen R E 2000 *Nature* **403** 281
[2] Noheda B, Cox D E, Shirane G, Gonzalo J A, Cross L E and Park S-E 1999 *Appl. Phys. Lett.* **74** 2059
[3] Noheda B, Gonzalo J A, Cross L E, Guo R, Park S-E, Cox D E and Shirane G 2000 *Phys. Rev.* B **61** 8687
[4] Noheda B, Cox D E, Shirane G, Guo R, Jones B and Cross L E 2001 *Phys. Rev.* B **63** 014103
[5] Noheda B, Cox D E, Shirane G, Gao J and Ye Z-G 2002 *Phys. Rev.* B **66** 054104
[6] Noheda B, Cox D E, Shirane G, Park S-E, Cross L E and Zhong Z 2001 *Phys. Rev. Lett.* **86** 3891
[7] Frantti J, Ivanov S, Eriksson S, Rundlöf H, Lantto V, Lappalainen J and Kakihana M 2002 *Phys. Rev.* B **66** 064108

[8] Topolev V Yu and Turik A V 2001 *J. Phys.: Condens. Matter* **13** 771
[9] Wilkinson A P, Xu J, Pattanaik S and Billinge S J L 1998 *Chem. Mater.* **10** 3611
[10] Larson A C and Von Dreele R B 2000 *General Structure Analysis System LANSCE* MS-H805, Los Alamos National Laboratory, Los Alamos, NM 87545
[11] Stephens P W 1999 *J. Appl. Crystallogr.* **32** 281
[12] Hill R J and Fischer R X 1990 *J. Appl. Crystallogr.* **23** 462
[13] Jansen E, Schäfer W and Will G 1994 *J. Appl. Crystallogr.* **27** 492
[14] Young R A (ed) 1996 *The Rietveld Method* (Oxford: Oxford University Press)
[15] Corker D L, Glazer A M, Whatmore R W, Stallard A and Fauth F 1998 *J. Phys.: Condens. Matter* **10** 6251
[16] Frantti J, Ivanov S, Lappalainen J, Eriksson S, Lantto V, Nishio S, Kakihana M and Rundlöf H 2002 *Ferroelectrics* **266** 73
[17] Frantti J, Lantto V, Nishio S and Kakihana M 1999 *Japan. J. Appl. Phys.* **38** 5679
[18] Souza Filho A G, Lima K C V, Ayala A P, Guedes I, Freire P T C, Mendes Filho J, Araújo E B and Eiras J A 2000 *Phys. Rev.* B **61** 14283
[19] Frantti J, Fujioka Y, Eriksson S, Lantto V and Kakihana M 2003 *Int. Conf. Electroceramics (Massachusetts Institute of Technology, Cambridge, USA, 3–7 August 2003)* at press
[20] Rogan R C, Üstündag E, Clausen B and Daymond M R 2003 *J. Appl. Phys.* **93** 4104
[21] Bedoya C, Muller Ch, Baudour J-L, Madigou V, Anne M and Roubin M 2000 *Mater. Sci. Eng.* B **75** 43